Structural and paleostress analysis within a fossil slow-spreading ridge: Tectonic processes involved during ocean expansion

Rémi Magott, Carole Berthod, Françoise Chalot-Prat

Structural and paleostress analysis within a fossil slow-spreading ridge: Tectonic processes involved during ocean expansion

Rémi Magott [a,*], Carole Berthod [b], Françoise Chalot-Prat [a]

[a] Centre de Recherches Pétrographiques et Géochimiques, Lorraine University, BP20, 15 Rue Notre Dame des Pauvres, F-54501, Vandoeuvre-les-Nancy Cedex, France
[b] Laboratoire Magma et Volcans, Clermont - Auvergne University, 6, Avenue Blaise Pascal, F-63178, Aubi`ere Cedex, France

This study aims to decipher the spatio-temporal chronology of tectonic processes leading to ocean widening at a slow-spreading oceanic ridge axis, involving mantle and gabbro exhumation and volcanism. Structural and petrographic studies of deformed lithologies were performed on peridotites, gabbros and basalts from the Chenaillet ophiolite (Alps, France). Inversion of fault-slip data reveals N030° and N060° σ_3 paleostress trends. The dominant N030° extension, is consistent with the NNW-SSE direction of volcano feeder-dykes and ENE dipping low-angle normal faults crosscutting the mantle. The N060° extension accords with the mantle dome structure formation to the east. Low-angle faults intersect roots of volcanoes that thus belong to their hanging walls. Hydrothermalism is contemporaneous with or postdates low-angle faulting. A feeder-dyke major virgation northwards, synchronous with eruptions, suggests a dextral transform fault consistent with a N120° σ_2. Oceanic expansion mechanisms are clarified. At the surface, magma eruption occurs along on-axis active high-angle normal faults, their footwalls enabling mantle exhumation. At depth, off-axis high-angle faults become low- angle faults as they spread at shallow level. With westward drift of the lithosphere, the uppermost levels of the ridge shift westward faster, such that volcanoes move to an off-axis position while their roots are cut by low- angle faults.

1. Introduction

Since the concept of oceanic spreading was first developed (Hess, 1962, 1965; Pitman et al., 1968), the process of surface creation along the mid-oceanic ridge plate boundary has remained rather enigmatic. For several decades, based on fast-spreading ridge lithological cross-sections, the surface creation was viewed as originating from magma injection at the ridge axis (Lonsdale, 1977, 1989; MacDonald, 1982; Whitehead et al., 1984; Detrick et al., 1987, 1993; MacDonald and Fox, 1988; Lin et al., 1990; Haymon et al., 1991; Scheirer and Macdonald, 1993; Perfit et al., 1994; Perfit and Chadwick, 1998). Very large volumes of magmas were thought to be emplaced both at depth and at the surface of the ridge axis, inducing surface enlargement with the lateral shifting of both plates. The underlying lithospheric mantle was understood to result from uninterrupted accretion of sub-solidus residues of asthenospheric partial melting producing MORB (Mid-Oceanic Ridge Basalts). The internal tectonic foliation of the lithospheric mantle was seen as developing from the fossilization of that acquired during upwelling asthenosphere up to the surface at the ridge (Rabinowicz et al., 1987; Ceuleneer et al., 1988; Nicolas et al., 1988; Nicolas and Boudier, 1995; Jousselin et al., 1998).

However the discovery in the mid 70's (FAMOUS expedition; Heirtzler and Van Andel, 1977) that lithospheric mantle outcropped extensively on the floor of the Mid-Atlantic ridge, whereas intrusive and extrusive magmatic rocks were rare or often absent, brought into question the role of magmas in the process of ocean enlargement. Indeed, on the seafloor of slow- but also fast-spreading ridges, sometimes over hundreds of kilometers as at the Arctic ridge (Michael et al., 2003) and in the Marianas back-arc basin (Stern et al., 1996; Ohara et al., 2002), magmatic products are completely absent, whereas there is an active widening of the peridotitic ocean floor. In other words, ocean widening can be significant without magma emplacement whether on the surface or at depth, and regardless of the spreading velocity. Nevertheless the scarcity or absence of crustal products on the seafloor of some active ridges, but also in many fragments of fossil oceanic ridges referred to as ophiolites, was initially viewed as abnormal until 30 years ago when it was reported that mantle outcropped almost all along the Atlantic ridge axis (Lagabrielle and Cannat, 1990).

* Corresponding author.)
E-mail addresses: remi.magott@gmail.com (R. Magott), carole.berthod@uca.fr (C. Berthod), francoise.chalot-prat@univ-lorraine.fr (F. Chalot-Prat).

Indeed magma genesis, in greater or lesser volumes, is synchronous with oceanic expansion without being the cause. Ocean enlargement results from the creation of oceanic floor surface by uninterrupted lithospheric mantle exhumation at the ridge axis, either directly at the ocean bottom at slow-spreading ridges, or below thick gabbro sill sequences at fast-spreading ridges. The self-consistent numerical model of Poliakov and Buck (1998) suggests that the creation of surface is due to continuous lithospheric mantle ascent at the axis from the Lithosphere-Asthenosphere Boundary (LAB), and lateral stretching of this mantle material on either side of the axis at large scale.

This process of "vertical uplift and lateral stretching" works even on a small scale (Fig. 7; in Poliakov and Buck, 1998) and leads to the formation of abyssal hills (hills carpeted with conic volcanoes) at the ridge axis. This process was proposed by Chalot-Prat (2005) to explain the construction of "comb volcanic systems" at a hectometric scale, in the Chenaillet mid-oceanic ridge fragment. These systems define reliefs where the higher the volcanic edifice, the younger it is relative to the others, a chronological emplacement mode also described at the Mid-Atlantic Ridge by Smith and Cann (1999). As volcanoes are built directly on uplifted mantle and never on top of each other, their successive construction traces mantle exhumation along high-angle normal faults.

On a larger scale, the model of Poliakov and Buck (1998) shows that on both sides of the ridge axis, both mantle upwelling and stretching processes lead to the formation of a complex pattern of convex-upward extensional faults deeply and vertically rooted below the axial valley. These are the detachment faults recognized and mapped for the past 20 years as low-angle faults at the top of oceanic core complexes (Whitney et al., 2013 and references therein). These core complexes are composed of mantle and intrusive gabbro sills exhumed at the surface as footwalls of detachment faults (Dick et al., 2003, 2019; Cannat et al., 2006; DeMartin et al., 2007; Escartín et al., 2008; Tucholke et al., 2008; Macleod et al., 2009; Miranda and Dilek, 2010; Maffione et al., 2013; Sauter et al., 2013; Parnell-Turner et al., 2018).

Finally, combining geophysical, petrological, and structural data on oceanic mantle lithosphere, Chalot-Prat et al. (2017) proposed an alternative oceanic plate spreading model in which detachment faulting is the major process to create the ocean floor surface leading to the widening of the ocean. In this last model, detachment faults result from intra-lithospheric mantle decoupling linked to the westward drift of the lithosphere (Cuffaro and Doglioni, 2007; Doglioni and Anderson, 2015; Doglioni and Panza, 2015).

It is critical to develop a better understanding of the tectonic processes acting during oceanic spreading. Deciphering these processes is less difficult at slow-spreading ridges, where the volumes of intrusive and extrusive magmas remain rather low. Over the past 30 years, oceanic prospecting campaigns have described large scale extensional structures and oceanic core complexes, especially along the Mid-Atlantic Ridge (MAR) and on the Southwest Indian Ridge (SWIR), (Karson, 1990; Tucholke and Lin., 1994; Tucholke et al., 1998; Blackman et al., 2008; Escartin et al., 2008; Macleod et al., 2009; Reston and Ranero, 2011; Hansen et al., 2013; Maffione et al., 2013; Dick et al., 2019 and references therein). However, knowledge of small-scale tectonic characteristics remains limited. Observed striations on convex-upwards surfaces of core-complexes are reported without any detailed description, making it difficult to develop an accurate idea of the stress associated with oceanic expansion. Moreover, the off-axis geometric and chronological relationships between the footwalls of low-angle faults, capping mantle and gabbroic basement, and their hanging walls supporting the volcanic cover and its underlying basement remains unknown.

This is why our study is focused on the description at different scales of brittle deformation structures within the mantle basement including gabbro sills and its volcanic cover from the Chenaillet ophiolite, a very well preserved fossil oceanic ridge fragment (Chalot-Prat, 2005; Chenaillet Ophiolite). We combined fault slip data, paleostress analysis, and field observations to develop a model for how this axial ridge fragment accommodated seafloor spreading. According to the field relationships between the three main lithologies, volcanic edifices were first built on a mantle basement experiencing uplift and exhumation in an on-axis position. At a larger scale, still on-axis but at shallow depth, low-angle faults developed crosscutting the roots of volcanoes that as a result are found in the hanging walls of low-angle faults. We finally establish a link and a clear timing between small-scale mantle exhumation synchronous with volcanic eruptions and large-scale mantle and gabbro exhumation related to low-angle normal fault activity. Hydrothermal deposits clearly post-date volcano building, and are contemporaneous with or postdate low-angle faulting.

2. Geological setting

The Chenaillet ophiolite (Franco-Italian Alps) is an undeformed fragment of an axial volcanic ridge of a slow-spreading ocean, active during the middle to upper Jurassic times (Chalot-Prat et al., 2003; Chalot-Prat, 2005; Chenaillet Ophiolite; Manatschal et al., 2011; Li et al., 2013). This oceanic ridge fragment was part of the Alpine Tethys ocean active between the European and Adriatic plates (Lemoine et al., 1987). It was obducted during ocean closure, thus escaped subduction and only recorded oceanic seafloor metamorphism (Chalot-Prat et al., 2003 and references therein).

It is preserved as a thrust sheet framed by 2 major faults SW-NE (Gidon, 1977; synthetic maps on the Gidon website Carte du Briançonnais septentrional). In Chalot-Prat (2005) and Chalot-Prat et al. (2006 Chenaillet Ophiolite), a 1:25,000 geological map, six related cross-sections, and many detailed observations of the lithological units, especially on volcano architectures, enable to identify the 3D geometry of a 30 km^2 portion including an abyssal hill, 18 km^2 in area, below and at the periphery of which is exposed a mantle basement intruded by gabbro sills (Fig. 1). On the whole, this small segment of an on-axis ocean floor is quite comparable to that described at the rift axis of the MAR (Mid-Atlantic Ridge).

In addition major element geochemistry confirmed that the whole basalts are tholeiitic. Their trace element signature was shown to be similar to Indian Enriched Mid-Oceanic Ridge Basalts (E-MORB).

The oceanic expansion was decrypted in studying the architecture of the volcanic cover (5–50 m thick) that looks like an abyssal hill with numerous hummocky ridges and hundreds of hummocks (small conic edifices) as described at the MAR. Mapping at 1:12,500 of volcanoes (5–50 m large and high, with conic or cascade shapes, with a central or lateral dyke) allowed identifying comb and stair volcanic systems, the first being largely dominant (90% of volcanoes). These comb systems (Fig. 14; in Chalot-Prat, 2005) define elongated reliefs (some hundreds of meters long and 100–150 m in elevation) where the higher the volcanic edifice, the younger it is relative to the others. Based on the relative chronology of setting up conic volcanoes and the 3D geometry of the comb systems, it was demonstrated that combs formed on a basement in uplift and exhumed progressively along high-angle detachment faults serving as magma conduits at depth and as a conveyor belt for hummocks on the seafloor to a limited extent ($<$500 m). Their building was, thus, synchronous with seafloor widening.

Furthermore, the undulated top of the mantle basement is capped with cataclasite horizons tracing the existence, at a kilometric scale, of low-angle detachment faults responsible for the exhumation of mantle core-complex on the eastern side of the abyssal hill, as detailed later by Manatschal et al. (2011). Apart from the fact that the only cross-section of this paper presents the pillow basalts as thick sedimentary deposits, only one mantle exhumation event is suggested before emplacement of the volcanic cover. Chalot-Prat (2005) suggested 2 successive exhumation events, before then synchronous with the building of comb systems. Indeed in many places, fine-grained clastic sediments, which consist exclusively of clasts deriving from erosion of mantle and gabbro basement, form lenticular and dislocated deposits below the bottom (the oldest volcanoes) of comb systems. These observations attest that mantle

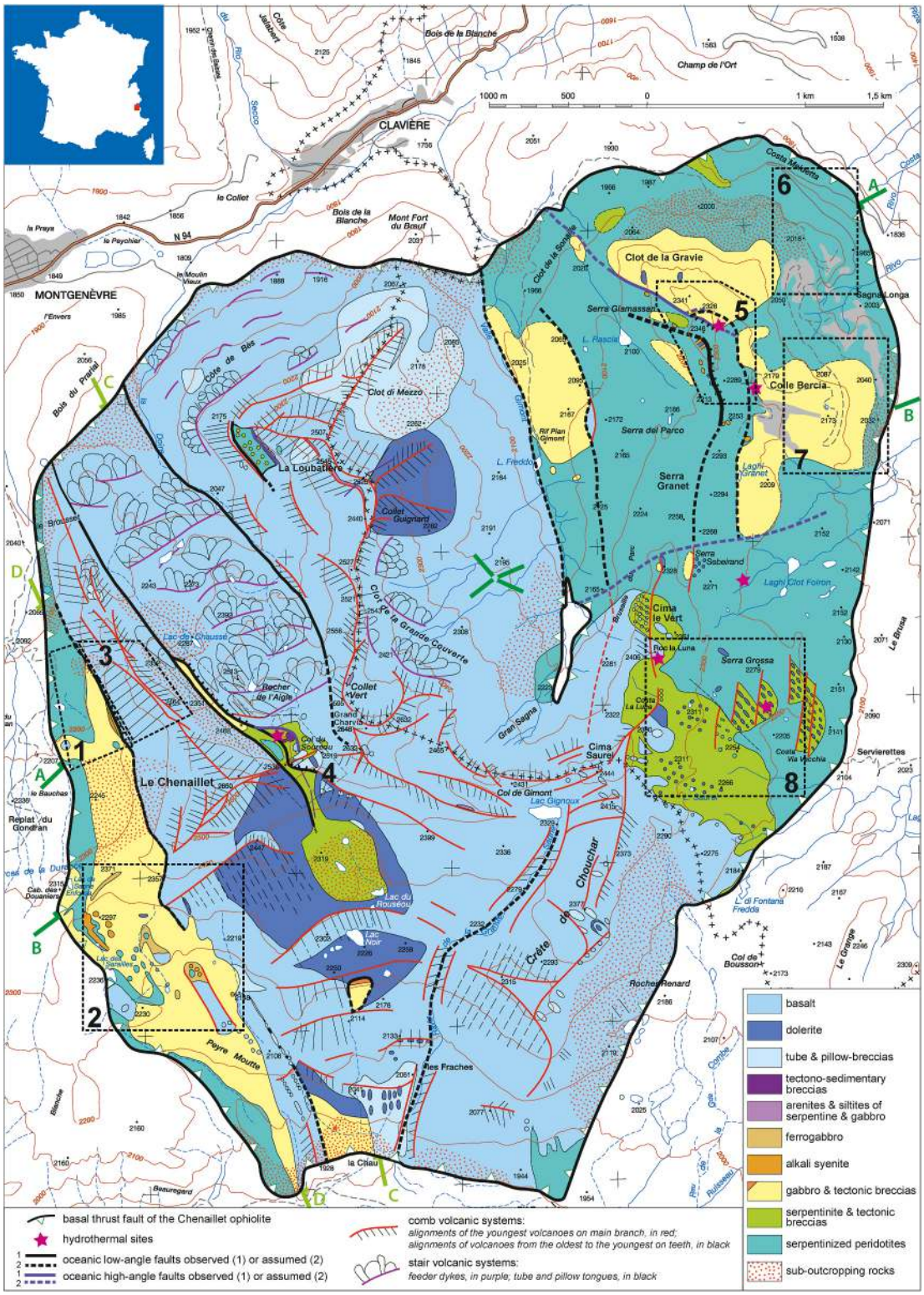

Fig. 1. (A). Geological map of the Chenaillet ophiolite (Western Alps; modified after Chalot-Prat, 2005). Purple segments A, B, C, D: location of 4 cross-sections of Fig. 1b. Dashed line frames: location of 8 studied sectors labelled 1 to 8. (b). Cross-sections in orthogonal directions of the Chenaillet ophiolite allowing visualization of the thinness (up to 50 m max) of both the volcanic cover and the gabbro sills capping a mantle basement crosscut by low-angle detachment faults. (For interpretation of the references to color in this figure legend, the reader is referred to the Web version of this article.)

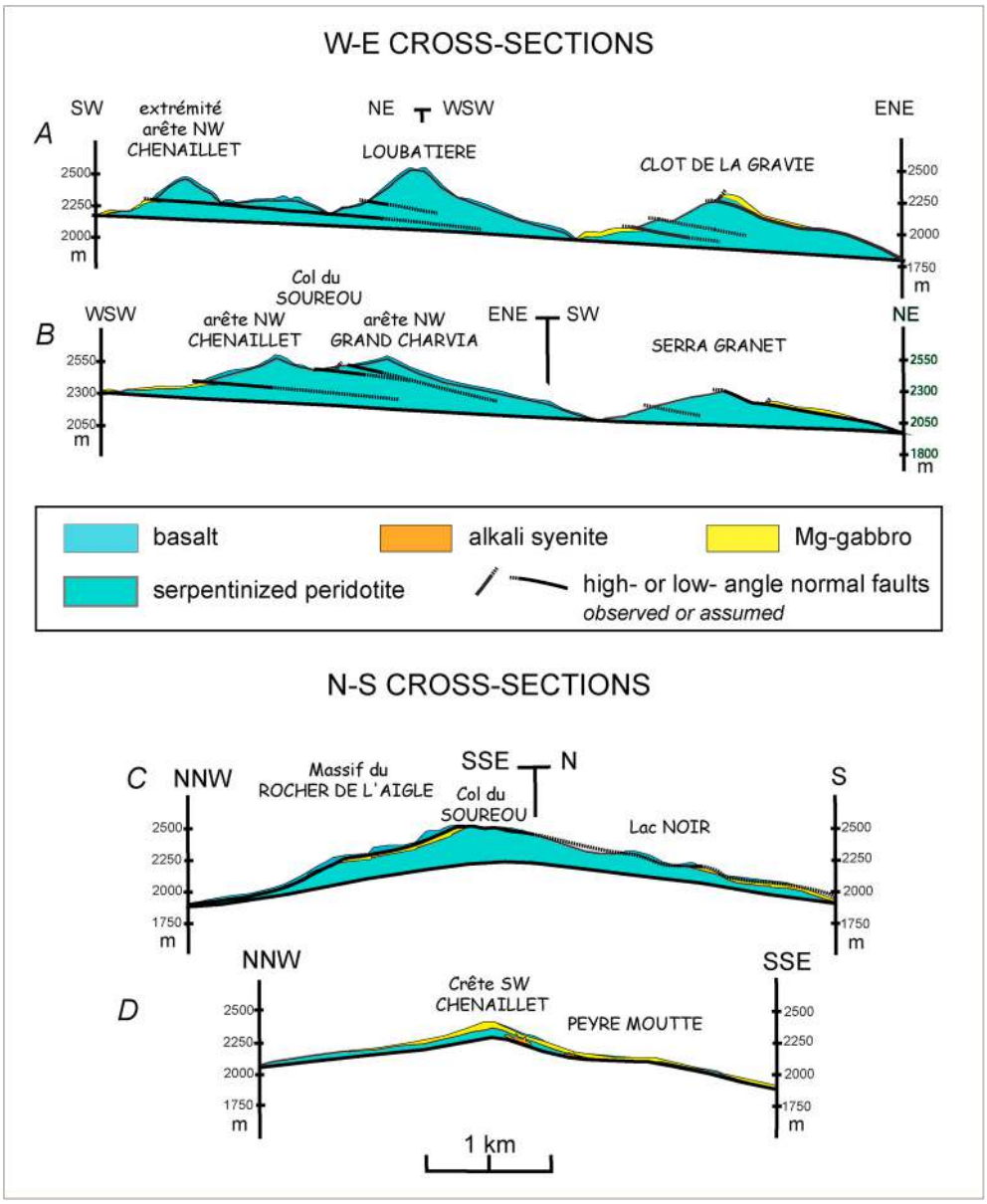

Fig. 1. (*continued*).

exhumation was already going on before initiation of the on-axis volcanic activity.

3. Results

3.1. Field observations

3.1.1. Structural analysis

This study focuses on the brittle deformation at the scale of the Chenaillet fossil oceanic ridge (Fig. 1a). In order to obtain the most accurate results, the studied area was divided in two main zones: a western zone, consisting of a mantle derived basement composed of serpentinized peridotite including gabbro sills, largely covered by basaltic volcanoes; an eastern zone with the same type of serpentinized peridotite/gabbro basement, but very partially covered with volcanoes and quite rich in hydrothermal deposits. Hereafter, we will use the term "basement" to qualify the mantle part of the Chenaillet unit. Each zone was subdivided in four sub-zones (1–4 in the western part and 5 to 8 in the eastern part) in order to obtain more accurate data in terms of lithology and geographic location.

The highlighted faults display a number of similarities. Most of them crosscut mantle rocks. Those who crosscut the volcanic edifices or only some pillow basalts, although present, are rarer and have always a small offset which never exceed several centimetres.

The faults cross-cutting the mantle-derived rocks can be grouped in two families. The first family corresponds to large low-angle faults, or detachment faults, at the scale of the unit. They are mainly oriented in a N–S axis with strikes between N160° and N175° and a weak dip which never exceeds 15°E (Figs. 1 and 2). These faults are commonly underlined by breccia horizons, 80 cm to 1 m thick, including angular to rounded serpentinite clasts embedded in a fine-grained serpentinite matrix. These breccias can locally be associated to calcite and serpentinite veins. Macroscopic kinematic indicators, like striated slickenside and C–S-like microstructures in cataclastic bands, always indicate a top-to-the-east sense of shear (Fig. 3). These detachment faults crosscut all other structures, including doleritic and basaltic dykes, especially in the sector 8.

The second family of faults has lowest extension, is rarely underlined

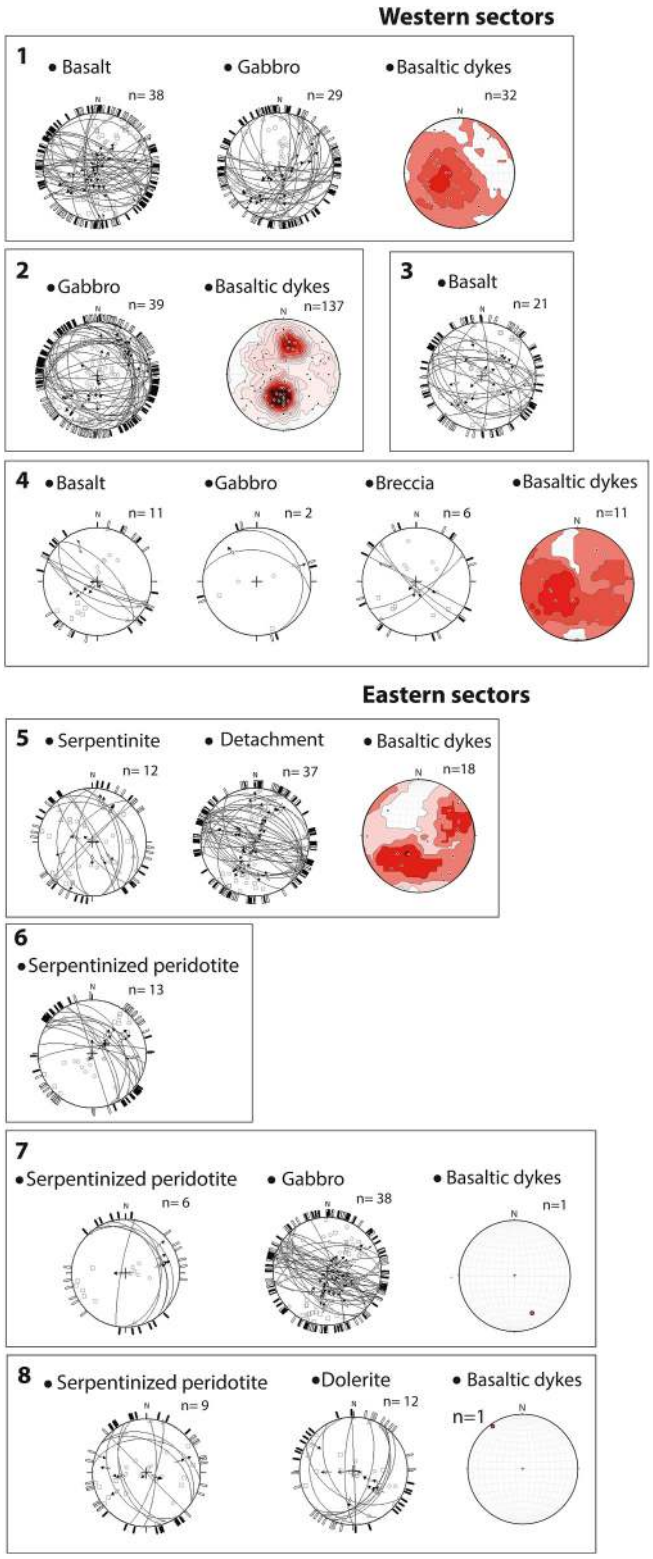

Fig. 2. Fault-slip data and related stress orientations. (a) For the 4 western sectors. (b) For the 4 eastern sectors. On the stereograms (equal area projections, lower hemisphere), red and blue arrows represent respectively the orientation of horizontal principal stresses σ3 (pointing outward) from extensional tensors and σ1 (pointing inward) from compressional tensors. The number of data used for each tensor is represented by n. (For interpretation of the references to color in this figure legend, the reader is referred to the Web version of this article.)

by breccia horizons and have more important dip angles (20°–85°, Fig. 2a and b). Their strikes and dips are more diversified than these of detachment faults. In the vast majority of cases, they have a normal kinematic, are rooted in the detachment faults or are conjugate faults of these low-angle faults. The largest faults can therefore display a noticeable deformed zone including breccia and/or fluid circulation indices. For example, in the sector 5 north-eastwards, the serpentinite – gabbro contact corresponds to a large rather high-angle fault (Fig. 4A, B and 4C). The many plans of faults measured allow determining two groups of plans (Fig. 2). The dominant group corresponds to the main fault, strikes N120° to N130° and dips around 50°S. Striation, close to N200°, is always associated with normal faulting. Near the main displacement plane, its conjugate faults strike N110° to N120° and dip 35° to 44°N. Striations are N050° to N150° and indicate also normal faulting.

Let note that although the vast majority of faults have normal kinematics, the eastern part of the Chenaillet unit (sector 7) is crosscut by faults that indicate two stages of faulting. The first stage normal faults strike N095° to N145° and dip 45°–70° NE. Related striation is N030° to N050° (Fig. 2). The second stage faults indicate a reverse kinematic crosscutting the kinematic indicators of the normal displacement. These two stages of faulting were observed mainly in gabbro, and in a lesser extent in mantle rocks.

Finally, a third family of faults crosscuts the volcano edifices. Our data come mainly from the sector 3, in the western part of the ocean fragment where outcrops a lot of adjoining conic volcanoes belonging to comb systems (Fig. 1a). Pillow-basalts are crosscut by metric scale faults (Fig. 2) forming two groups, the second one being a conjugate of the first: 1- striking N100° to N140° and dipping 54° to 80°NE. Striation is rather homogeneous N055° to N065° associated with a top-to-the-north; 2- striking N095° to N160° and dipping 15° to 40°SW. Striation, N220 to N250°, is associated with normal faulting. All displacements along these faults are short and never exceed centimetres to decimetres.

In addition to the observation of the brittle deformation structures, this study focused on the attitude of the basaltic to doleritic dykes within the basement. These dykes (n = 137) are striking N090° to N130° and clustered in two groups according their dip and the direction of the dip (Fig. 2; Table 1): 1- dipping 30°–65° NE; 2- dipping 40°–55° S. It is worth to note that vertical dykes within the basement remain rare whatever the sector studied, while volcano feeder dykes (same diameter and composition than those within the basement) within all the volcanic edifices are always vertical or close to the vertical (Chalot-Prat, 2005; Chenaillet Ophiolite).

3.1.2. Hydrothermalism and fluid-rock interactions

Several sites testify to hydrothermal circulations in the Chenaillet mid-oceanic ridge section (Figs. 1a and 5). Most of them occur in the eastern zone, mostly along or close to fault contacts between gabbro and serpentinized peridotite (*Clot de la Gravie* to *Colle Bercia*), or close to main branch (=feeder dykes) of comb systems (*Cima le Vert* and *Serra Grossa*). With only a single site along a detachment fault (*Col du Souréou*), the western part mostly covered with volcanoes is devoid of any hydrothermal circulation witness. In the eastern zone, two types of hydrothermalized sites (Fig. 5) are identified either with siliceous veins or only whitish and deeply weathered. The siliceous type results from the circulation of Si-rich fluid along high-angle fault planes (Figs. 5 and 6). Centimeter-scale corrugated quartz veins, located along the fault plane, are concentrated in the most deformed zone of the fault system and crosscut all microstructures of brittle deformation, especially the gabbro breccia, but also basaltic dykes (Fig. 6A and B). Noticeable pervasive silicification occurs on 2–3 m thick on each side of the fault plane, permeating both foliated serpentinite and cataclastic gabbro. These veins are parallel to fault planes at N110°; 78° N. However undeformed gabbro remains well preserved. Besides, some quartz thin veins underline the contact between serpentinite and the wall of a basaltic dyke (sector 8 on Fig. 1a). These veins crosscut sometimes the

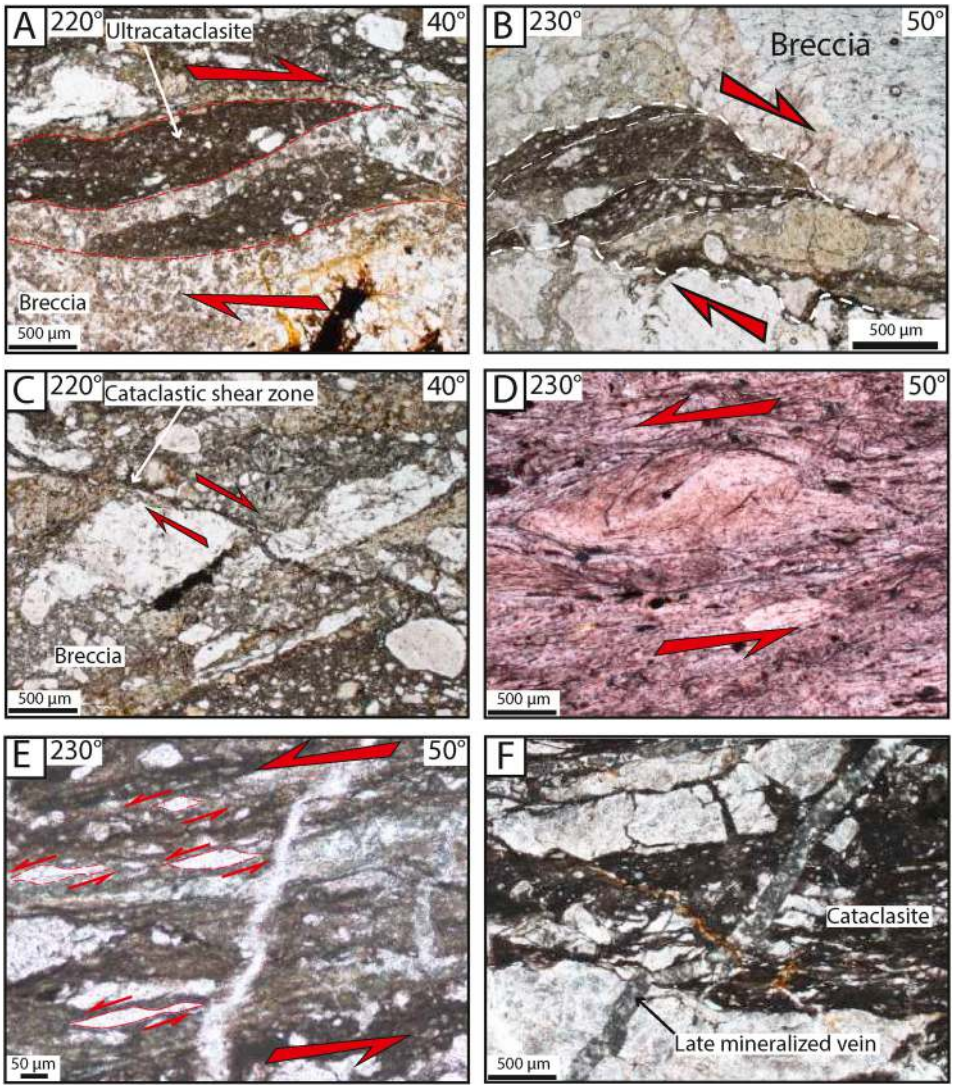

Fig. 3. Observation of kinematic indicators and cross-cutting relationships in thin sections within highly deformed rocks sampled along e E-dipping low angle fault (Sector 1) and a W-dipping fault (Sector 5). (A) Ultracataclasite S–C microstructures indicating a top-to-the-NE embedded in a cataclasite shear band (Sector 1). (B) Ultracataclasite S–C microstructure along sector 1 low-angle fault indicating a top-to-the-NE displacement? (C) Cataclastic zone reworked by a top-to-the-NE micro-fault (sector 1). (D) S–C microstructure indicating a top-to-the-SW in highly deformed silicified serpentinite fault zone (Clot de la Gravie fault – sector 5). (E) S–C deformation indicating a top-to-the-SW in the cataclastic gabbro (Clot de la Gravie fault – sector 5) Late hydrothermal vein crosscutting the deformation. (F) Crosscutting relationships between cataclastic deformation in the sector 1 gabbro and late hydrothermal circulation.

basaltic dyke on a few centimeters. Siliceous veins are also observed in sector 5 and the western part of sector 8 through small extension veins (<10 cm) crosscutting basaltic dykes (Fig. 1a). The second type of sites mainly outcrops within sector 8. The mantle host-rock and pillow-lavas underwent hydrothermal alteration identified by a whitish color linked to a strong weathering of primary minerals transformed into white to clear brown clay minerals (Fig. 6C). These alterations superpose each time to fault systems. The weathering is pervasive and homogeneous on 5 m thick of the hanging wall and less than 2 m thick of the footwall. On *Cima le Vert* (Fig. 1) strikes and dips are N042°; 62° W to N060; 55° N. Moreover in the western zone of the oceanic fragment, another and unique type of Ca-rich hydrothermal site outcrops within the uppermost part of the serpentinized mantle at the *Col du Souréou* (sector 4; Fig. 1a). This site is located at the intersection of a major east-dipping low-angle fault and a conjugate high-angle fault (Fig. 1a) and was identified as a tectonic-sedimentary breccia oriented N020° to N030°; 50° E (Chalot-Prat, 2005 and references therein). The rock, named ophicalcite, consists of a brecciated serpentinized peridotite associated with authigenic calcite within a matrix composed of fine-grained calcite (Lafay et al., 2017). The breccia is also crosscut by late-stage dolomite micro-veins. This ophicalcite of *Le Souréou* would represent a larger volume of hydrothermal fluid while being unique within this oceanic ridge fragment. This context is rather different from this observed in the eastern zone where hydrothermal deposits are rather common but scattered, suggesting circulation of weak hydrothermal fluid volumes.

In summary at the scale of this oceanic lithosphere fragment, hydrothermal sites are always located along normal low-angle or/and high-angle faults within mantle rocks. Most of them are located in zones mostly devoid of any volcanic activity. In many cases, these fluid circulations crosscut basaltic dykes when they exist, and thus postdate the volcanic eruptions.

3.2. *Paleostress analysis*

3.2.1. *Materials and methods*

The structural study concerns two main zones within the Chenaillet axial ridge fragment (Fig. 1a). Each of them includes 4 measurement sectors: a western zone with the sectors 1 to 4 and an eastern zone with the sectors 5 to 8. Each zone includes the best outcrops of mantle and gabbro basement on these very steep (800 m height difference from 1850 to 2650 m above sea level) slope where the Chenaillet unit was mapped. The different sectors concern separate studying sites adjoining each other. Data include more than 300 striated fault planes, which crosscut serpentinized peridotites, gabbros, and pillow basalts. The wall direction of basaltic lava dykes crosscutting gabbro and serpentinized peridotite was also measured and their dip as well. The slip direction is determined by striation and associated sense of slip, which was established by conventional kinematic analysis of brittle microstructures

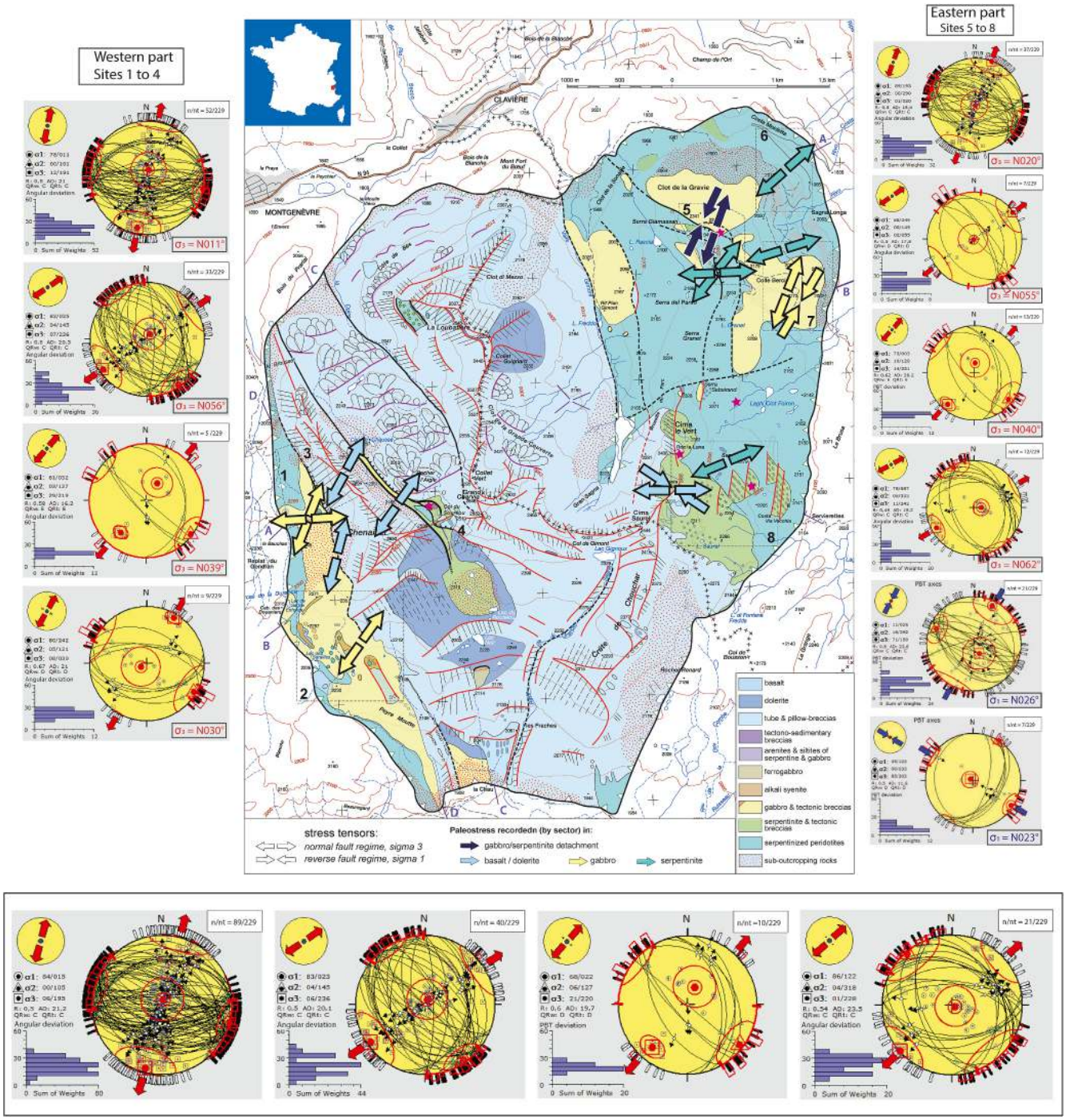

Fig. 4. (A) Respective orientation of σ3 (pointing outward) and σ1 (pointing inward) from tensors calculated on the geological map of the Chenaillet ophiolite. The tensors at left were calculated from faults in the western part of the unit and the tensors at right were calculated from faults located on the eastern part of the unit. (b) Tensor calculated from all faults at the scale of the entire unit.

(Hancock, 1985; Petit, 1987; Passchier and Trouw, 2005). Kinematic along faults is established with two methods at different scales: 1- at a macroscopic scale, the observation of indicators (offsets, S–C like microstructures, plowing and Riedels micro-faults) along the fault zones are observed and measured; 2- at a microscopic scale, the observation of kinematic indicators in thin section made perpendicularly to the displacement plane and parallel to the striation or lineation, within highly deformed rocks sampled along fault zones.

The striated fault planes were used to determine the paleostress axis with the inversion principle initially developed by Wallace (1951) and Bott (1959) and improved by several authors (Angelier, 1975, 1979, 1990, 1991; Célérier, 1988; Etchecopar et al., 1981; Dupin et al., 1993; Delvaux and Sperner, 2003). Inversion of fault slip data in stress tensor implies that the maximum computed shear stress along a fault plane is parallel to the slip direction observed in the outcrop. Furthermore, a fault plane has an orientation that allows the relative magnitudes of shear stress τ and normal stress σ on this plane to fit the Mohr-Coulomb yield criterion: $\tau = c + \mu\sigma$ (c: shear strength; μ: coefficient of friction). According to these mechanical laws, stress inversion techniques search for the state of stress that best accounts for a given fault-slip dataset by iteratively adjusting the theoretical slip pattern associated with a known stress state until it fits the slip pattern observed at the outcrop (Angelier,

Table 1
Main parameters of the dykes measured in sectors 1 to 8 (with both our data and those of Coco and Bastien (Master dissertation - ENSG-CRPG/CNRS, 2003; unpublished).

Sector 1			Sector 2 (Continued)			Sector 2 (Continued)			Sector 2 (Continued)		
Azimuth	Dip	Dip direction	Azimuth	Dip	Dip direction	Azimuth	Dip	Dip direction	Azimuth	Dip	Dip direction
Coco and Bastien data											
0	20	E	100	40	NE	80	10	NW	80	40	SE
0	15	E	90	30	N	20	85	NW	80	70	SE
100	20	NE	90	35	N	90	60	S	80	70	SE
110	55	NE	90	40	N	90	70	S	160	90	W
110	40	NE	100	40	NE	30	50	SE	320	76	E
110	80	NE	100	40	NE	30	50	SE	340	30	E
120	20	NE	100	65	SW	35	15	SE	275	55	N
130	60	NE	100	50	SW	50	40	SE	160	75	W
160	50	NE	100	30	NE	80	40	SE			
100	20	NE	100	20	NE	80	70	SE	***Sector 4***		
160	60	NE	100	40	SW	100	40	SW	**Azimuth**	**Dip**	**Dip direction**
170	50	NE	100	50	SW	100	30	SW	*Our data*		
40	40	NW	100	40	SW	110	40	SW	350	40	E
80	30	NW	100	20	SW	110	40	SW	120	60	S
25	60	NW	110	30	NE	110	40	SW	195	55	W
60	70	NW	110	30	NE	110	60	SW	215	78	W
60	60	NW	110	30	NE	120	40	SW	6	52	E
20	40	SE	110	30	NE	120	60	SW	134	62	S
70	70	SE	110	50	NE	150	50	sw	344	40	E
80	30	SE	110	30	SW	160	60	SW	322	40	E
30	50	SE	110	30	NE	180	70	W	240	62	N
30	50	SE	110	50	NE	180	70	W	282	25	N
60	80	SE	110	50	SW	90	20	N			
130	75	SW	110	50	SW	90	50	N	***Sector 5***		
130	70	SW	110	30	SW	90	50	N	**Azimuth**	**Dip**	**Dip direction**
135	80	SW	120	80	SW	90	60	N	*Coco and Bastien data*		
150	10	SW	120	50	NE	100	30	NE	180	80	E
150	10	SW	130	45	SW	110	40	NE	120	50	NE
0	90		130	10	NE	110	40	NE	120	50	NE
Our data			130	40	NE	120	80	NE	120	30	NE
315	65	N	130	45	NE	160	20	NE	140	40	NE
30	39	E	140	65	NE	50	30	NW	30	15	NW
18	32	E	140	80	SW	80	40	NW	30	60	NW
			150	40	NE	80	10	NW	60	80	NW
Sector 2			150	75	NE	90	60	S	60	70	NW
Azimuth	**Dip**	**Dip direction**	150	50	NE	90	70	S	80	30	NW
Coco and Bastien data			150	50	NE	30	50	SE	40	60	SE
20	20	SE	160	20	NE	30	50	SE	140	40	SW
30	50	SE	160	50	NE	50	40	SE	140	80	SW
40	20	SE	170	60	NE	100	40	SW	140	60	SW
40	40	SE	180	35	W	100	30	SW	170	60	SW
40	40	SE	180	30	E	110	40	SW	Our data		
40	40	SE	90	20	N	110	40	SW	160	65	W
40	70	NW	90	50	N	110	40	SW	310	64	N
40	50	NW	90	50	N	110	60	SW	230	76	N
50	70	NW	90	20	N	120	40	SW			
50	60	SE	90	60	N	120	60	SW	***Sector 7***		
60	25	NW	100	30	NE	150	50	sw	**Azimuth**	**Dip**	**Dip direction**
70	25	NW	110	40	NE	160	60	SW	Our data		
80	50	SE	110	40	NE	180	70	W	245	63	N
80	60	NW	120	80	NE	180	70	W			
90	30	N	160	20	NE	90	20	N	***Sector 8***		
90	30	N	10	40	NW	10	40	NW	**Azimuth**	**Dip**	**Dip direction**
90	45	N	50	30	NW	20	85	NW	Our data		
90	30	N	80	40	NW	35	15	SE	55	85	S

1979; Etchecopar et al., 1981; Angelier et al., 1982).

Considering these parameters, the orientation of the principal stress axes σ_1, σ_2 and σ_3, with $\sigma_1 \geq \sigma_2 \geq \sigma_3$ (in positive compression) and the stress ratio $R=(\sigma_2-\sigma_3)/(\sigma_1-\sigma_3)$ are adapted for minimize the α angle or misfit angle. This is the angle between the maximum calculated shear stress and the measured slip direction for a fault plane.

In this study, the ''TENSOR'' software (Delvaux and Sperner, 2003) was used to perform the stress inversion and determine the paleostress. This program, for a given set of fault slip data, enables to compute the best fitting stress tensor. The process consists of a rotational

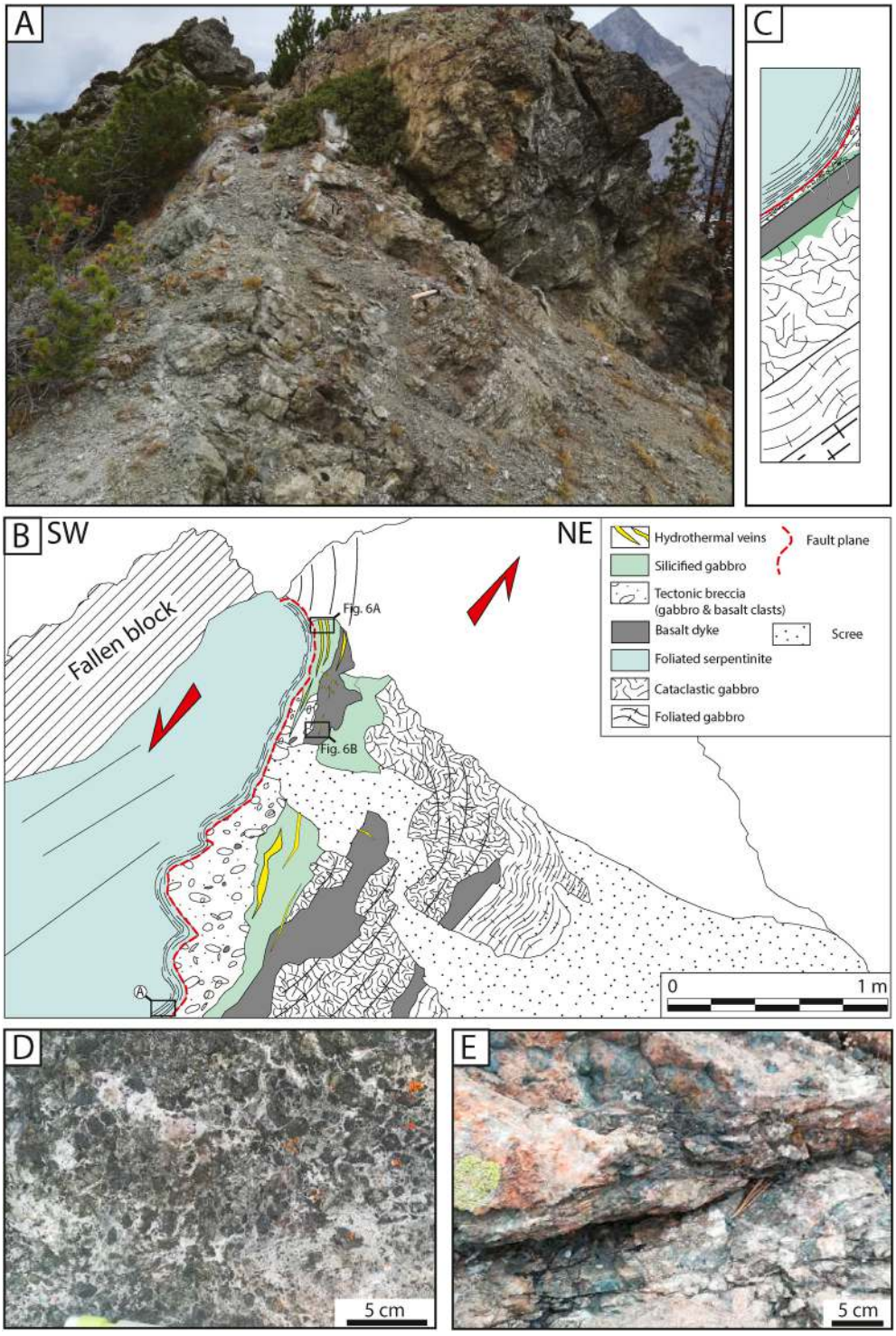

Fig. 5. Description of La Gravie high-angle fault system. (A) Tectonic contact, along a high-angle fault, between gabbro and serpentinite units (site 5; Clot de la Gravie). (B) Sketch of the outcrop showing cataclasites or foliated-cataclasites in the gabbro. (C) Cross-section of the fault zone and deformed fault zone in the gabbro and serpentinite blocks. (D) Serpentinite breccia highlighting the deformation along large low-angle fault in sector 4 between gabbroic footwall and serpentinite hangingwall. (E) Serpentinite breccia associated to the low-angle fault crosscutting the sector 5.

optimization, an iterative procedure by which the best result is determined by an incremental rotation of the stress tensor until obtaining the best solution relatively to the observed fault slip data. The value of the final computed stress tensor reflects the number of data, their quality, and the value of the misfit angle α. It is important to underline that no hypothesis is made on the attitude of fault planes relative to stress axes. Whether a fault plane is newly created, or is instead a reactivated pre-existing discontinuity, has no consequence for the calculation of the paleostress tensor.

Inversion was then computed on consistent individual sub-sets, and the quality of the results was checked through the misfit criteria previously mentioned. All incompatible data with a given stress tensor ($\alpha > 30^\circ$, for example) were associated with another data sub-set or, if incompatible with any stress tensor, moved to the waste database. The process was repeated until a unique and stable stress tensor was obtained to give a consistent sub-set. All stress tensors are associated with a relative chronology of fault slips and associated with major structures when crosscutting relationships between kinematic indicators can be observed.

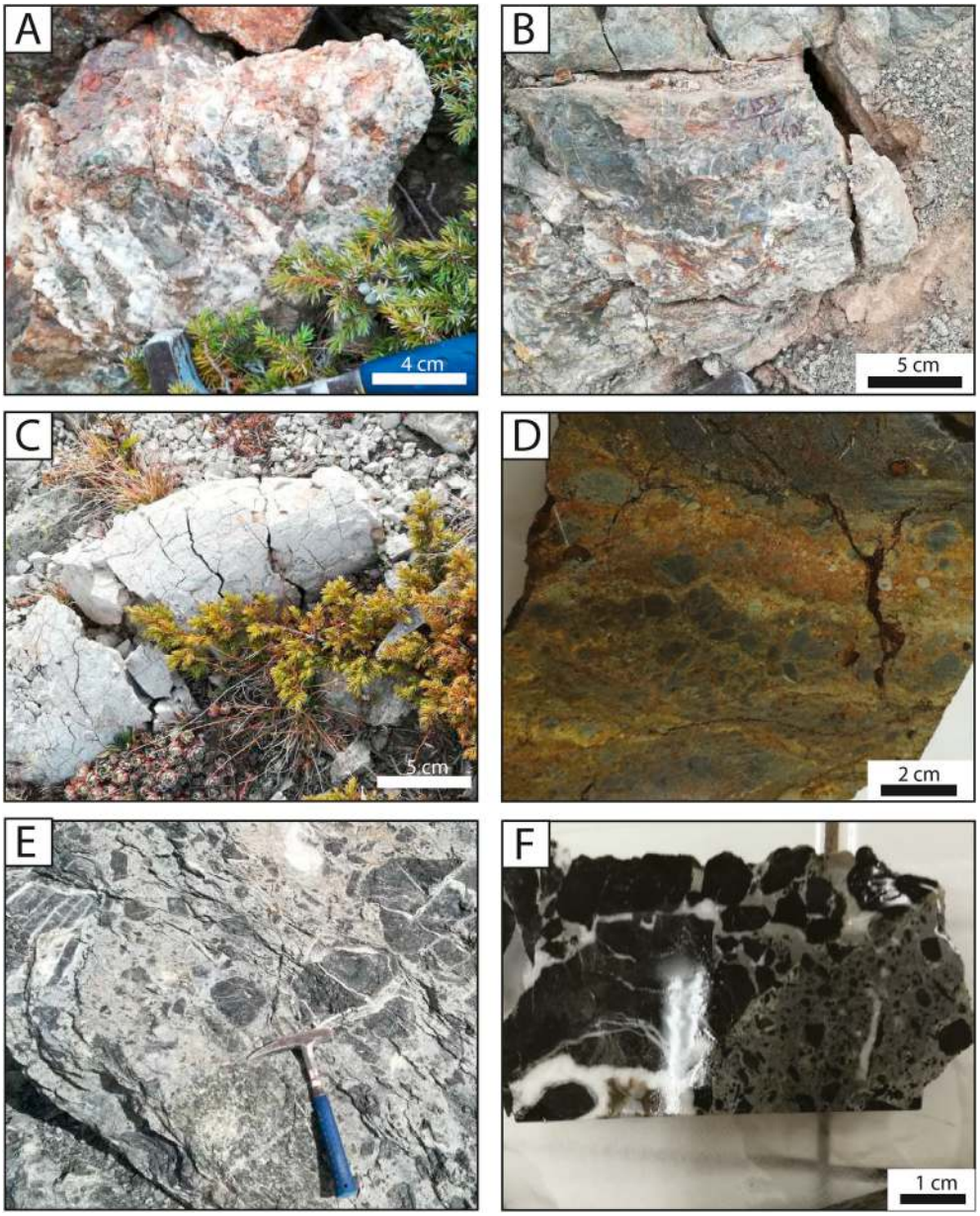

Fig. 6. Fluid circulation imprints on rocks. (A) Centimetre-scale corrugated quartz veins, located along the La Gravie fault (Sector 5). (B) Basaltic dykes crosscut by quartz veins along La Gravie fault. (C) Weathered pillow. (D) Polished hand sample of weathered basalt. Most of primary minerals are substituted by clay minerals and serpentine. (E) Ophicalcite observed at the Col du Souréou (site 4; east of the Chenaillet peak). (F) Polished hand sample of ophicalcite crosscut by late stage dolomite microveins.

3.2.2. Results

Approximately 270 fault-slip data were collected from the 8 sectors (1–8; Fig. 1a) and more precisely in 41 punctual measurement sites, together with striations, conjugate faults, and basaltic dykes. In several locations, especially in the eastern zone (sectors 6 and 7), overprinted slickensides were observed.

The stress tensors were calculated for the entire western and the eastern zones. All paleostress data computed with the numerical program stress 'TENSOR' (Table 2) are reported in Figs. 2 and 4. The large majority of studied sites include a sufficient number of data to compute paleostress for each sector, leaving few isolated data.

All tensors were firstly calculated from fault data set subdivided by lithology and measurement site. For the sake of precision, the colored arrow on the map of Fig. 4 represents the main direction of σ_3 for each sector (1–8) with consideration for lithology. Then, all tensors were calculated from fault data independently of the lithology and site (Fig. 4b and Table 3).

On the western part, four tensors have been obtained from the fault data. A first subset of mostly neoformed faults striking N075° to N125° and deep 10°N to 30°S yields a NNE – SSW direction of σ_3 at N011° associated to striation between N005° and N050° or N155° to N210° (Fig. 4a). A second extensional stress tensor considers neoformed faults striking N125° to N175° and dipping 30°E to 30°W (Fig. 4a). Calculation indicates a direction of σ_3 at N056° associated to striation between N055° and N070° (Fig. 4a). These two extensional stress tensors concentrate the majority of the data.

The two other tensors involve less data (Fig. 4a). The third subset of reactivated faults striking N110° to N135° and deep 60°N to 50°S yield an extensional stress tensor with the σ_3 oriented N039°. However, striation associated to these faults strike mainly N060° (between N050° and N070°). The last extensional stress tensor indicates a σ_3 striking N030°. It was calculated from reactivated faults striking N140° to N150° and dipping 30°E to 40°E with striation close to N030° (between N025° and N030°).

In the eastern part of the unit, six stress tensors could be calculated from the structural data. Four of them indicate a main sub-horizontal extension stress and two indicates compressional stress. The first of them have been obtained from neoformed faults striking between N080°

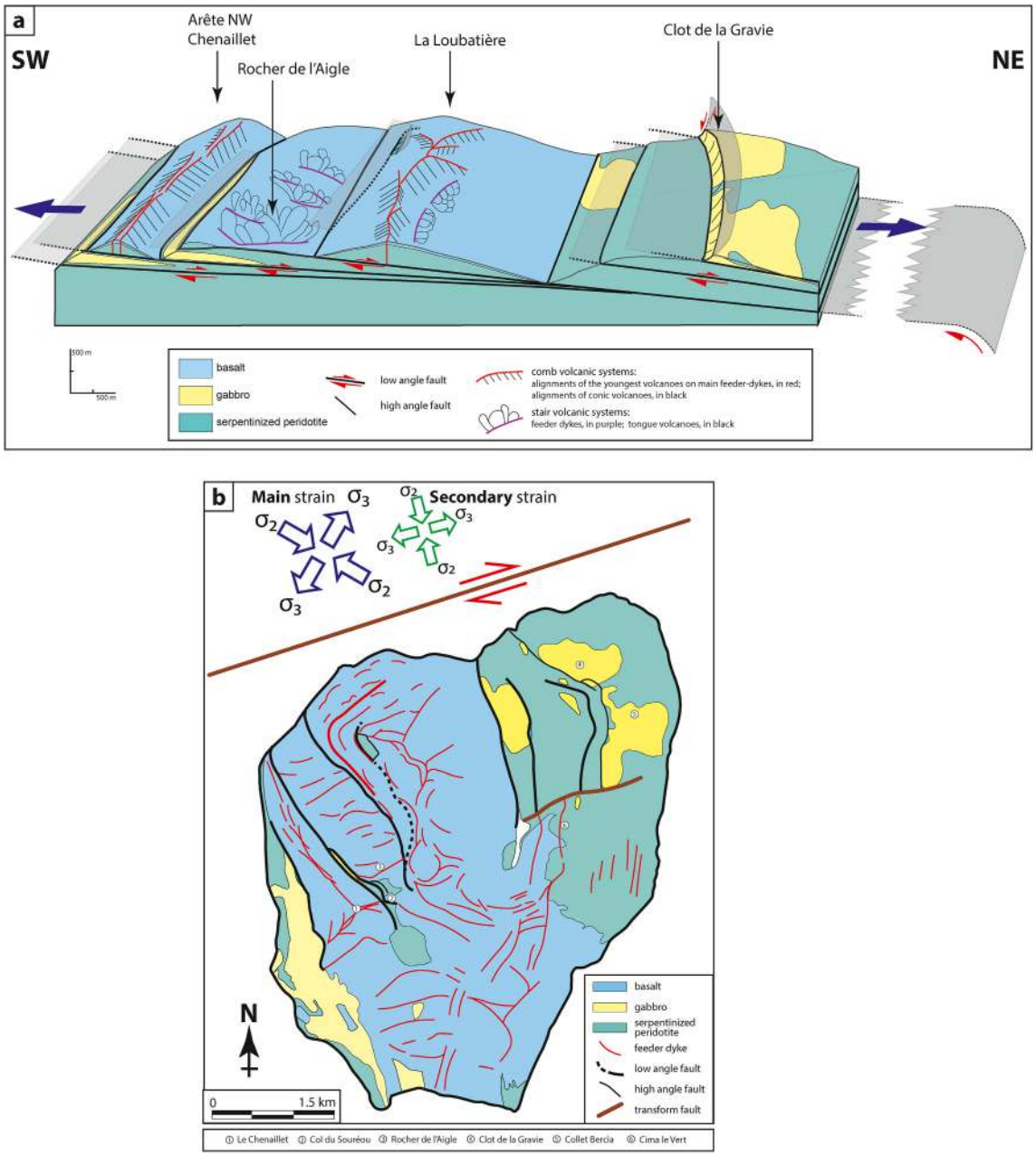

Fig. 7. (A) Schematic 3D cross-section of the half northern part of le Chenaillet unit (along B section. (b) Synthetic tectonic map implying a large strike-slip fault north to the unit.

to N135° and dipping 20°N to 45°S. The associated σ_3 is calculated at N020°. Striation observed in these faults is close to the direction of σ_3 with direction between N355° and N040°, and between N170° to N210°. A second subset of neoformed faults striking N130° to N190° and deep 25°E to 40°SW, associated to striation between N050° and N075°, yield an extensional stress tensor with the σ_3 oriented N055° (Fig. 4a).

Two other extensional stress tensors imply less data. The third stress tensor includes reactivated faults striking between N130° to N150° and dipping 30°N to 40°S. The associated σ_3 is calculated with fault data at N40°, but striation is clustered between N050° to N070° indicating an extensional direction at N60°. Conversely, the fourth tensor is calculated from a subset of reactivated faults striking N125° to N150° and dipping 30°E to 50°E with striation direction between N010° to N035°. This indicates a first σ_3 direction at N062° during the formation of the faults followed by a reactivation with a σ_3 at N30° as attested by the orientation of the striations.

Finally, two tensors indicate the horizontal compressional regime after the first extensional regime. A first well documented tensor, localized only in the sector 5 and 7, indicates a σ_1 at N026° compression phase postdating all extensional stages. It was calculated from faults striking between N090° to N165° and dipping 20°NE to 40°SW. Striations are between N345° to N030°, and N190° to N230° (Fig. 4a). A second tensor, with less data, indicates a compressive tectonic phase, only in the sector 8, with σ_1 at N123° from faults striking between N010° and N050° and dipping between 40°E to 60°E. All striation is clustered around N290°.

At the scale of the entire unit, four tensors were calculated as shown on Fig. 4b. The first tensor includes faults striking N060° to N130° and dipping 15°–85° north or south. Striations are between N350° to N45° or N150° to N210°. The main extensional direction σ_3 is N020°. The second tensor displays a σ_3 striking N060° with faults striking N125° to N175° and dipping 20°–80° NE or 35° to 85°SW. Striations is between N040°

Table 2
Paleostress tensors computed from fault data. NF (normal fault) and TF (thrust fault) stand for normal and thrust fault regimes. R = (σ2 - σ3)/(σ1 - σ2). AD (angular deviation) between each data and all the calculated nuclei. QRw and QRt are quality estimators, ranging from A (best) to E (worst), of paleostress orientations and of the R ratio, respectively.

Site	Lithology	Stress regime	Strike/dip sigma 1	Strike/dip sigma 2	Strike/dip sigma 3	R	AD	QRw	QRt	n/nt
Sector 1	Basalte	NF	N306/83°	N104/06°	N194/03°	0.5	27	C	C	26/38
	Gabbro	NF	N359/77°	N110/05°	N201/12°	0.5	23.4	D	D	15/29
	Gabbro	NF	N343/70°	N178/19°	N086/05°	0.44	23.6	D	D	10/29
Sector 2	Gabbro	NF	N048/81°	N305/02°	N215/09	0.42	23.2	C	C	34/39
Sector 3	Basalte	NF	N170/84°	N298/04°	N028/05°	0.5	21.6	C	C	10/21
Sector 4	Basalte	NF	N025/57°	N022/05°	N215/33°	0.5	12.3	E	E	7/11
Sector 5	Gabbro/serpentinite Detachment	NF	N277/88°	N109/01°	N019/01°	0.5	19.1	C	C	24/37
	Gabbro/serpentiniteDetachment	TF	N205/10°	N295/04°	N044/79°	2.5	18.1	D	D	7/37
	Serpentinite	NF	N352/70°	N125/14°	N218/15°	0.57	16.6	E	E	5/13
	Serpentinite	NF	N178/59°	N356/31°	N087/01°	0.34	28.9	D	D	6/13
Sector 6	Serpentinite	NF	N206/79°	N317/04°	N048/11°	0.5	15.3	C	E	10/13
Sector 7	Serpentinite	NF	N081/72°	N343/03°	N252/18°	0.46	13.4	E	E	6/6
	Gabbro	NF	N050/79°	N292/05°	N201/10°	0.5	23.4	C	C	16/38
	Gabbro	TF	N030/21°	N291/22°	N159/59°	2.5	21.4	C	C	14/38
Sector 8	Serpentinite	NF	N045/88°	N157/01°	N247/02°	0.52	15.6	D	D	6/9
	Dolérite	NF	N284/79	N179/03°	N089/10°	0.5	24.3	E	E	4/12
	Dolérite	TF	N123/05	N033/00°	N303/85°	2.5	11.6	D	D	7/12

Table 3
Paleostress tensors computed from fault data independently of the lithology.

Site	Lithology	Stress regime	Strike/dip sigma 1	Strike/dip sigma 2	Strike/dip sigma 3	R	AD	QRw	QRt	n/nt
Sectors 1 - 4	Basalte and gabbro	NF	N011/78°	N101/00°	N191/12°	0.5	21	C	C	52/266
	Basalte and gabbro	NF	N025/82°	N145/04°	N236/07°	0.5	20.3	C	C	33/266
	Basalte and gabbro	NF	N032/61°	N127/03°	N219/29°	0.5	16.2	E	E	5/266
	Basalte and gabbro	NF	N242/80°	N121/05°	N030/08°	0.67	21	D	D	9/266
Sectors 5 - 8	Gabbro, serpentinite and dolerite	NF	N193/89°	N290/00°	N020/01°	0.5	19.4	C	C	37/266
	Gabbro, serpentinite and dolerite	NF	N249/88°	N145/00°	N055/02°	0.5	17.8	D	D	7/266
	Gabbro, serpentinite and dolerite	NF	N003/73°	N128/10°	N221/14°	0.62	20.2	E	E	5/266
	Gabbro, serpentinite and dolerite	NF	N087/78°	N333/05°	N242/11°	0.46	15.2	C	C	12/266
	Gabbro, serpentinite and dolerite	TF	N026/11°	N292/16°	N150/71°	0.5	23.8	C	C	21/266
	Gabbro, serpentinite and dolerite	TF	N123/05°	N033/00°	N303/85°	0.5	11.6	D	D	7/266
All sectors	All lithologies	NF	N015/84°	N105/00°	N195/06°	0.5	21.2	C	C	89/266
	All lithologies	NF	N023/83°	N145/04°	N236/06°	0.5	20.1	C	C	40/266
	All lithologies	NF	N022/68°	N127/06°	N220/21°	0.6	19.7	D	D	10/266
	All lithologies	NF	N122/86°	N318/04°	N228/01°	0.54	23.5	C	C	21/266

and N085°. The third tensor indicates a σ_3 striking N050° with faults striking N135° to N180° and dipping 30° to 45°NE or 50 to 88°SW. Striations are oriented N010° to N030°. The last and fourth tensor indicates a σ_3 at N050° calculated from faults striking N110° to N175° and dipping 30° to 60°N or 35° to 55°S. Striation orientations are clustered between N045° and N070°.

4. Discussion

4.1. Paleostress interpretations

The microtectonic study indicates a dominant σ_3 paleostress direction close to N030° (Fig. 4b) within the whole ocean fragment. A secondary extension is computed close to N060°. No chronology clue is observed between the kinematic indicators associated with each of them.

Nevertheless, the presence of faults formed under a N030° extension regime, but reactivated by a N060° extension regime as evidenced by the strike of striations around N060°, suggests a change in the stress field from N030° to N060°. However other faults, formed under a N060° extensional regime but displaying N030° striations, suggest, conversely, a change in the stress field from N060° to N030°. That suggests that both paleostress trends were active successively, considering that the N060° σ_3 would have induced the formation of the dome structure capped by a curved and upward convex low-angle fault (Fig. 1 b A and 1 b B; Fig. 7a and b). The intermediate σ_3 directions (N30/50/70), computed on localized parts of the map and represented by arrows in Fig. 4a, within this area support that assumption. That confirms that the whole "*Clot de la Gravie - Serra Granet*" area is a small oceanic core-complex (≈3 km^2), as already suggested by Chalot-Prat (2005) and Manatschal et al. (2011).

Furthermore, as observed on the N–S cross-sections (Fig. 1b), the base of the Chenaillet ocean fragment is itself upward-convex, thus merges with a detachment fault at around 400–500 m depth below the seafloor (Chalot-Prat, 2005). So the Chenaillet ophiolite is itself a mantle slice, some tens of km^2 of surface, belonging to the hanging wall of this basal major detachment fault.

A synthetic 3D-reconstitution of the northern half of the ocean fragment (Fig. 7a) shows that the peridotitic and gabbroic basement of this ocean fragment is crosscut by a bundle of major low-angle faults dipping to the east, fairly tight between them (not more than 30 m

between each). They are observed in both orthogonal directions as shown by the SW-NE cross-sections (Figs. 1b and 7a). Several conjugate faults of these detachment faults (Figs. 1a and 7) are at the origin of preserved cliffs (up to 50 m high on 300 m to 2.5 km long) within the mantle, as at the mantle-gabbro contact west of *Clot de la Gravie*, and as north of *Col du Souréou*. Here tectono-sedimentary breccia (Lagabrielle and Cannat, 1990) are witnesses to the activity of one of these conjugate faults.

Rather thin gabbro sills (up to 50 m thick on 1 km long) were exhumed from place to place either at surface eastwards or below volcanic edifices westwards. The volcanic edifices and their related mantle basement always belong to the hanging wall (up to 200 m thick only) of detachment faults.

Furthermore as described in Chalot-Prat (2005), at large scale west and north to the *Loubatière peak* (northern central part of the Chenaillet unit; Fig. 1a), a large virgation (elbow-shaped curvature) in the alignments of feeder-dyke networks is observed from N060° to N140°. This eastward virgation was contemporaneous of basaltic eruptions, because of the preservation of original shapes of volcanic edifices (tongues and cones of tubes and pillows). It could be linked to a strike-slip fault located north of the unit (Fig. 7b) and oriented around N060° (±20°) with a dextral kinematic, implying the opening of feeder-dykes synchronously with the formation of the strike-slip fault. The assumed N060° strike of this major fault is consistent with the N030° σ_3 direction and an assumed σ_2 direction around N120 (Fig. 7b) considering the regional paleostress calculations. Similar volcanic system organizations were already observed close to transform faults on the North Atlantic mid-oceanic ridge (Gudmundsson, 1995; Beutel, 2005). Notice that previous mapping results (Gidon, 1977 and Gidon website Carte du Briançonnais septentrional) show, both north and south of the Chenaillet ophiolite, two strike-slip faults with a similar strike than that northern transform fault evidenced in this study. This would mean that another transform fault would exist south of this oceanic fragment (outside the map Fig. 1a). These faults would have facilitated the individualization, without any deformation, of the obducted oceanic fragment during the ocean closure. Let note that accounting for the reconstruction of the western Tethyan region (Turcot et al., 2012), this fossil ocean fragment would have rotated approximately 45° counterclockwise from its initial position.

In addition, two convergent paleostress directions at N020° (predominant) and N120° (less frequent) are computed only in the eastern zone (Fig. 4a). All associated striations and slickensides always post-date extensional regime kinematic indicators. In the absence of any paleostress analysis in the units underlying the Chenaillet ophiolite, it remains difficult to associate these fault reactivations with a special event. However regarding the crosscutting relationships between normal kinematic indicators, late compressive indicators, and the weakness of the offsets, this convergent event could be reasonably related to the obduction of the oceanic ridge fragment.

The southern part of this ridge fragment has not yet been the subject of a detailed structural analysis and should bring interesting results on the N–S spreading process accounting for the W-E numerous feeder-dykes of the mapped comb systems.

4.2. Volcanic edifices and mantle-gabbro core complexes are tracers of spreading both on and off-axis; how does seafloor enlargement occur?

As evidenced in Fig. 7a showing the relationships between major tectonic structures, the feeder-dykes of both comb and tongue volcanic systems are always crosscut at depth (down to 50–150 m) by low-angle faults. The presence of basaltic clasts within cataclasite breccia along these faults supports this conclusion. So all volcanic activity was definitively stopped when detachment faults progressively developed at shallower depth, laterally to the ridge axis, preventing any ascent and eruption of basaltic magma up to the seafloor.

However, from detailed observations of sharp to plastic contacts of numerous basaltic feeder-dykes crosscutting gabbro bodies (Chalot-Prat, 2005; Manatschal et al., 2011), it is demonstrated that basaltic magma was injected within gabbro bodies either while gabbroic rocks were still plastic and even still incompletely crystallized at rather great depth, or close to the surface while gabbro bodies were completely crystallized, rigid, and often strongly foliated.

That means that at the ridge axis, during the permanent upwelling of mantle and intrusive gabbroic bodies, basaltic magma could be injected through these host-rocks at any time and any level between the base of the lithosphere and the seafloor. This also suggests that tectonic constraints, enabling upwards transfer and foliation of peridotite and gabbro, could coexist with those inducing cracking of these more or less rigid host-rocks and injection of basaltic magma from below the base of mantle lithosphere (>30 km mini.; Chalot-Prat et al., 2010, 2013) up to the oceanic bottom. Only the development of the curvature of detachment faults at shallow depth laterally to the ridge axis (Chalot-Prat et al., 2017) could prevent any basaltic melt progression to the surface and stop any volcano building.

At the same time as these low-angle faults lead to mantle and gabbro exhumation in their footwalls, they induced the renewal of the basement of previously formed mantle reliefs (up to 500 m thick) covered with volcanoes, but without any spreading effect. In return in the northeastern part of the oceanic fragment (*Clot de la Gravie* to *Serra Granet*), where volcanic edifices were very rare, detachment faults induced mantle and gabbro sills exhumation forming a core-complex on the bottom of the ocean, thus seafloor enlargement on some km2.

At this stage of the demonstration, it is worth remembering that the emplacement of volcanoes in comb volcanic systems (90% of volcanic systems; Fig. 1a) is itself strictly linked to mantle exhumation (Chalot-Prat, 2005). Indeed, conic volcanoes formed on slopes, and the higher the edifice the younger it is relative to the others. Combs formed on a basement in uplift and in the process of denudation along high-angle detachment faults serving first as magma conduits beneath the ocean floor, then as a conveyor belt for volcanoes on the seafloor to a limited extent (<500 m) (Fig. 14, in Chalot-Prat, 2005). By the fact, the seafloor enlargement accompanied the building of volcanic edifices, the basement of which was the newly created surface by mantle exhumation. That creation of surface during the volcanic activity was linked to upwards then lateral mantle transfers operating at a small scale at the axis of the ridge and inducing the formation of new rather small elongated reliefs covered by conic volcanoes organized in comb systems. The whole relief, capped by a few hundred volcanic edifices, is the abyssal hill that represents most of the Chenaillet ophiolite.

Notice in the eastern zone of the oceanic ridge fragment (Fig. 1a), the juxtaposition between sites where mantle exhumation, thus creation of surface, occurred southwards along high-angle normal faults associated with the construction of volcanoes (*Costa via Vecchia - Serra-Grossa*), and northwards along low-angle normal faults (*Serra Granet - Clot de la Gravie*). The directions of high- and low-angle faults are in continuation of each other, while their respective dips are so different. Nevertheless, to the north, gabbroic sills (*Colle Bercia*) that belong to the hanging wall of a low-angle normal fault, were transferred to the east, whereas to the south, volcanoes were sliding east during the construction of comb systems. This coherence in both the fault directions and the relative movement along the faults on both sides suggests a contemporaneity of fault activity within the same stress context. However from either side, the mode of mantle exhumation is radically different. It implies the existence of an ENE-WSW rather deep vertical fault between both, parallel to that of the transform fault to the north. This reinforces the hypothesis of the major role of the N030° direction of σ_3 implying a N120° direction of σ_2, for initiating and controlling the activity of these faults (Figs. 1a & 7b).

The numerical model of Poliakov and Buck (1998) gives very interesting ideas both on the surface and depth effects, at small and large scales, of mantle mass transfer processes: on one hand at the ridge axis with the coeval formation of small mantle reliefs as abyssal hills on-axis,

and on another hand farther laterally of mantle core-complexes. Indeed, below the small reliefs on-axis, it shows that mantle transfers coming from the base of the lithosphere remain vertical till the surface, then laterally develop at the surface on both sides of the relief. At large scale, mantle transfer paths progressively curve outward away from the axis at any level from the base to the top of mantle lithosphere. In the brittle domain at shallower depth, major faults become individualized while overlapping the curved paths of mantle transfer. The curvature of these mantle transfer paths would be induced both by spreading and intra-mantle decoupling linked to the westward drift of the lithosphere (Chalot-Prat et al., 2017).

Hydrothermal circulations were active during and after low-angle fault emplacement, never during the volcanic eruptions. That could be linked to the slowness of the low-angle fault activation process, strictly linked to upward and lateral mantle mass transfer process, the rate of which is the half-spreading one (hS); for instance, for hS = 2 cm/yr and a mantle residue initial depth of Di = 40 km, the mantle residue takes t1 2 Ma (t1 = Di/hS) to ascend and to be exhumed at the surface (Chalot-Prat et al., 2017), which gives time to fluids to be extracted from the mantle in process of serpentinization from about 8 to 10 km depth (Mallows and Searle, 2012; Whitney et al., 2013). This slowness of propagation of low-angle faults from an on-to off-axis position, explains why all the basaltic dykes within the basement are all tilted while the feeder-dykes inside the volcanic edifices are all more or less vertical.

Finally, the major result of this study is to emphasize the possible relationships in space and time between high- and low-angle detachment fault individualization, mantle exhumation, volcanic system formation, and core-complex development. Comb volcanic systems form along high-angle faults at the ridge axis, are then transferred laterally whereas their roots are crosscut by low-angle faults. These low-angle normal faults first renew the mantle basement from a few hundred meters under the volcanoes, then outcrop at the surface where the volcanic edifices are absent and create themselves surface giving birth to core complexes. This would explain why at active mid-oceanic ridges, most of core complexes are found on the outskirts of the volcanic ridge axis, and sometimes at the axis when volcanic systems are absent.

5. Conclusions

The detailed structural and paleostress analysis within the fossil slow-spreading ridge fragment of the Chenaillet ophiolite leads us to greatly deepen our knowledge not only of the tectonic structure of this oceanic ridge fragment, but also of the combination of processes operating at the ridge axis and the timing of events to create seafloor.

The mantle basement of this ridge fragment appears to be crosscut by a bundle of low-angle normal faults dipping eastwards. A thin volcanic cover (up to 50 m) on its basement caps the uppermost one. The deepest and the most extensional one is the basal thrust fault of the Chenaillet ophiolite. Their arch shape in N–S direction suggests that when spreading was active, this ocean fragment (5 km in width) was isolated between two transform faults north- and south-wards. The existence of the one in the north is constrained by the nearby large virgation of basaltic feeder-dykes synchronous with eruptions and by our structural analysis. Conjugate high-angle normal faults are rather frequent and determine active cliffs, sometimes associated with tectono-sedimentary breccia deposits.

Combining all the fault data, two paleostress trends of σ_3, N030° and N060° are emphasized (Fig. 4b). The dominant σ_3 striking N030° is consistent with the general organization of both the feeder-dykes of volcanic systems and all of the low-angle faults. It fits also with the existence of the transform fault to the north, itself parallel to a fault separating the *Cima Le Vert* unit from the *Serra Granet* unit. The subordinate σ_3 striking N060°, identified only in the eastern part of the ocean fragment, is associated with the formation of the dome structure of the *Clot de la Gravie - Colle Bercia - Serra Granet* core complex. All these deformations occurred within the same extensional paleostress context, which induced ocean spreading.

Furthermore in this slice of the upper oceanic mantle represented by the Chenaillet ophiolite, at one hundred meters deep, low-angle normal faults intersect everywhere roots of volcanoes, which thus belong to their hanging wall. So the end of the volcanic activity coincided with the westward off-axis emplacement of low-angle faults. In addition both the volcanic abyssal hill and the eastward peridotitic and gabbroic core complex have been slightly laterally transferred off-axis westwards to become the hanging walls of deeper detachment faults. This would be the effect of the permanent westward drift of the lithosphere, whose shifting velocity decreases from top to bottom due to the asthenospheric mantle eastward flowing, which induces in turn the internal mantle decoupling and the detachment fault genesis at all scales at shallow level (Chalot-Prat et al., 2017).

Notice that activity of the low-angle faults did not disturb at all the coherence of the numerous volcanic systems with respect to each other within the abyssal hill, while hundreds of conic and in cascade volcanoes retained their original geometry (Chalot-Prat, 2005). This suggests that the block movement along any detachment fault concerns mainly its footwall, leading to the lateral transfer of the mantle to the west and its exhumation to the ocean seafloor when the volcanic cover is absent. Thus this laterally exhumed basement has not the same age as the volcanoes above and is much older, because the migration ridge velocity Vr is always higher than the half-spreading one hS.

6. Data availability statement

The data used to support the findings of this study are included within the article.

7. Authorship contributions

Please indicate the specific contributions made by each author (list the authors' initials followed by their surnames, e.g., Y.L. Cheung). The name of each author must appear at least once in each of the three categories below.

Category 1.

Conception and design of study: Rémi Magott, Carole Berthod; acquisition of data: Rémi Magott, Carole Berthod; analysis and/or interpretation of data: Rémi Magott, Carole Berthod, Françoise Chalot-Prat.

Category 2.

Drafting the manuscript: Rémi Magott, Françoise Chalot Prat, Carole Berthod revising the manuscript critically for important intellectual content: Rémi Magott, Françoise Chalot Prat, Carole Berthod.

Category 3.

Approval of the version of the manuscript to be published (the names of all authors must be listed): Rémi Magott, Françoise Chalot Prat, Carole Berthod.

Declaration of competing interest

The authors declare that they have no competing financial interests or personal relationships that could have appeared to influence the work reported in this paper.

Acknowledgements

The authors are grateful to the CRPG (our lab) for its financial support for the three field campaigns necessary to collect the structural data and to allow brainstorming meetings between the authors of this paper. This research did not receive any specific grant from funding agencies in the public, commercial, or not-for-profit sectors. This manuscript has benefited greatly from the detailed and always constructive reviews by Dr Jeremy Deans and 3 other anonymous reviewers that we sincerely thank. We warmly thank Laurie Reisberg for her precious help on the

English form of the text. This is the CRPG-CNRS contribution no. 2708.

References

Angelier, J., 1975. Sur l'analyse de mesures recueillies dans des sites faillés : l'utilité d'une confrontation entre les méthodes dynamiques et cinématiques. C. R. Acad. Sci. 281, 1805–1808.

Angelier, J., Goguel, J., 1979. Sur une méthode simple de détermination des axes principaux des contraintes pour une population de failles. C. R. Acad. Sci. 288, 307–310.

Angelier, J., Lybéris, N., Le Pichon, X., Barrier, E., Huchon, P., 1982. The tectonic development of the Hellenic arc and the Sea of Crete: a synthesis. Tectonophysics 86 (1–3), 159–196.

Angelier, J., 1990. Inversion of field data in fault tectonics to obtain the regional stress – III. A new rapid direct inversion method by analytical means. Geophys. J. Int. 103, 363–376.

Angelier, J., 1991. Inversion directe et recherche 4-D : comparaison physique et mathématique de deux modes de détermination des tenseurs des paléocontraintes en tectonique de failles. C. R. Acad. Sci. 312 (10), 1213–1218.

Beutel, E.K., 2005. Stress-induced seamount formation at ridge-transform intersections. In: Foulger, G.R., Natland, J.H., Presnall, D.C., Anderson, D.L. (Eds.), Plates, Plumes, and Paradigms, vol. 388. Geological Society of America Special Paper, pp. 581–593. https://doi.org/10.1130/2005.2388(34.

Blackman, D.K., Karner, G.D., Searle, R.C., 2008. Three-dimensional structure of oceanic core complexes: effects on gravity signature and ridge flank morphology, Mid-Atlantic Ridge, 30° N. G-cubed 9 (6).

Bott, M.H.P., 1959. The mechanisms of oblique slip faulting. Geol. Mag. 96 (2), 109–117.

Cannat, M., Sauter, D., Mendel, V., Ruellan, E., Okino, K., Escartín, J., Combier, V., Baala, M., 2006. Modes of seafloor generation at a melt-poor ultraslow-spreading ridge. Geology 34 (7), 605–608. https://doi.org/10.1130/G22486.1.

Célérier, B., 1988. How much does slip on a reactivated fault plane constrain the stress tensor. Tectonics 7, 1257–1278.

Ceuleneer, G., Nicolas, A., Boudier, F., 1988. Mantle flow patterns at an oceanic spreading centre: the Oman peridotites record. Tectonophysics 151 (1–4), 1–26.

Chalot-Prat, F., Ganne, J., Lombard, A., 2003. No significant element transfer from the oceanic plate to the mantle wedge during subduction and exhumation of the Tethys lithosphere (Western Alps). Lithos 69, 69–103. https://doi.org/10.1016/S0024-4937(03)00047-1.

Chalot-Prat, F., 2005. An undeformed ophiolite in the Alps: field and geochemical evidence for a link between volcanism and shallow plate tectonic processes. In: Foulger, G.R., Natland, J.H., Presnall, D.C., Anderson, D.L. (Eds.), Plates, Plumes, and Paradigms, vol. 388. Geological Society of America Special Paper, pp. 751–780. https://doi.org/10.1130/2005.2388(43.

Chalot-Prat, F., Falloon, T.J., Green, D.H., Hibberson, W.O., 2010. An experimental study of liquid compositions in equilibrium with plagioclase + spinel lherzolite at low pressures (0.75 GPa). J. Petrol. 51 (11), 2349–2376.

Chalot-Prat, F., Falloon, T.J., Green, D.H., Hibberson, W.O., 2013. Melting of plagioclase +spinel lherzolite at low pressures (0.5 GPa): an experimental approach to the evolution of basaltic melt during mantle refertilisation at shallow depths. Lithos 172–173, 61–80.

Chalot-Prat, F., Doglioni, C., Falloon, T., 2017. Westward migration of oceanic ridges and related asymmetric upper mantle differentiation. Lithos 268 (271), 163–173. https://doi.org/10.1016/j.lithos.2016.10.036.

Cuffaro, M., Doglioni, C., 2007. Global kinematics in deep versus shallow hotspot reference frames. In: Foulger, G.R., Jurdy, D.M. (Eds.), Plates, Plumes, and Planetary Processes, vol. 430. Geological Society of America Special Paper, pp. 359–374. https://doi.org/10.1130/2007.2430(18).

Delvaux, D., Sperner, B., 2003. New aspects of tectonic stress inversion with reference to the TENSOR program. Geological Society, London Special Publication 212 (1), 75–100.

DeMartin, B.J., Sohn, R.A., Canales, J.P., Humphris, S.E., 2007. Kinematics and geometry of active detachment faulting beneath the Trans-Atlantic Geotraverse (TAG) hydrothermal field on the Mid-Atlantic Ridge. Geology 35 (8), 711–714. https://doi.org/10.1130/G23718A.1.

Detrick, R.S., Buhl, P., Vera, E., Mutter, J., Orcutt, J., Madsen, J., Brocher, T., 1987. Multi-channel seismic imaging of a crustal magma chamber along the East Pacific Rise. Nature 326, 35–41.

Detrick, R.S., Harding, A.J., Kent, G.M., Orcutt, J.A., Mutter, J.C., Buhl, P., 1993. Seismic structure of the southern east pacific rise. Science 259, 499–503.

Dick, H.J.B., Lin, J., Schouten, H., 2003. An ultraslow-spreading class of ocean ridge. Nature 426, 405–412.

Dick, H.J., Kvassnes, A.J., Robinson, P.T., MacLeod, C.J., Kinoshita, H., 2019. The atlantis bank gabbro massif, southwest Indian ridge. Progress in Earth and Planetary Science 6 (1), 1–70.

Doglioni, C., Anderson, D.L., Anderson, L., 2015. Top Driven Asymmetric Mantle Convection. The Interdisciplinary Earth: A, Volume. Geological Society of America Special Paper 514, American Geophysical Union Special Publication 71. http://dx.doi.org/10.1130/2015.2514(05).

Doglioni, C., Panza, G.F., 2015. Polarized plate tectonics. Adv. Geophys. 56 (3), 1–167. https://doi.org/10.1016/bs.agph.2014.12.001.

Dupin, J.-M., Sassi, W., Angelier, J., 1993. Homogeneous stress hypothesis and actual fault slip: a distinct element analysis. J. Struct. Geol. 15, 1033–1043.

Escartín, J., Smith, D.K., Cann, J., Schouten, H., Langmuir, C.H., Escrig, S., 2008. Central role of detachment faults in accretion of slow-spreading oceanic lithosphere. Nature 455, 790–795. https://doi.org/10.1038/nature07333.

Etchecopar, A., Vasseur, G., Daignieres, M., 1981. An inverse problem in microtectonics for the determination of stress tensor from fault striation analysis. J. Struct. Geol. 3, 51–56.

Gidon, M., 1977. Carte géologique simplifiée des Alpes occidentales, du Léman à Digne, au 1/250.000°. Editions DIDIER & RICHARD et B.R.G.M., carte (2 feuilles) et notice, p. 18.

Gudmundsson, A., 1995. Stress fields associated with oceanic transform faults. Earth Planet Sci. Lett. 136, 603–614. https://doi.org/10.1016/0012-821X(95)00164-8.

Hancock L, P, 1985. Brittle microtectonics: principles and practice. J. Struct. Geol. 7 (3–4), 437–457.

Hansen, L.N., Cheadle, M.J., John, B.E., Swapp, S.M., Dick, J.B., Tucholke, B.E., Tivey, M.A., 2013. Mylonitic deformation at the Kane oceanic core complex: implications for the rheological behavior of oceanic detachment faults. G-cubed 14 (8). https://doi.org/10.1002/ggge.20184.

Haymon, R., Fornari, D.J., Edwards, M.H., Carbotte, S., Wright, D., Macdonald, K.C., 1991. Hydrothermal vent distribution along the East Pacific Rise crest (9°09'-54'N) and its relationship to magmatic and tectonic processes on fast-spreading mid-ocean ridges. Earth Planet Sci. Lett. 104, 513–534.

Heitzler, J.R., Van Andel, T.H., 1977. Project FAMOUS: its origin, programs and setting. Geol. Soc. Am. Bull. 88 (4), 481–487.

Hess, H.H., 1962. History of ocean basin. Petrologic Studies 599, 620.

Hess, H.H., 1965. Mid-ocean ridges and tectonics of the sea floor. In: Whitard, W.F., Bradshaw, R. (Eds.), Submarine Geology and Geophysics: Proceedings of the 17th Symposium of the Colston Research Society. Butterworths, London, pp. 317–334.

Jousselin, D., Nicolas, A., Boudier, F., 1998. Detailled mapping of a mantle diaper below a paleo-spreading center in the Oman ophiolite. J. Geophys. Res. 103 (B8), 18153–18170.

Karson, J., 1990. Seafloor spreading on the Mid-Atlantic Ridge: implications for the structure of the ophiolites and oceanic lithosphere produced in slow-spreading environments. In: Oceanic Crustal Analogues, Proceedings of the Symposium TROODOS 1987. Geological Survey Department, Nicosia, Cyprus.

Lafay, R., Baumgartner, L.P., Schwartz, S., Picazo, S., Montes-Hernandes, G., Vennemann, T., 2017. Petrologic and stable isotopic studies of a fossil hydrothermal system in ultramafic environment (Chenaillet ophicalcites, Western Alps, France): processes of carbonates cementation. Lithos 294–296, 319–338.

Lagabrielle, Y., Cannat, M., 1990. Alpine Jurassic ophiolite resemble to modern central Atlantic basement. Geology 18, 319–322.

Lemoine, M., Tricart, P., Boillot, G., 1987. Ultramafic and gabbroic ocean floor of the Ligurian Tethys (Alps, Corsica, Apennines): in search of a genetic model. Geology 15, 622–625.

Li, Xian-Hua, Faure, M., Lin, W., Manatschal, G., 2013. New isotopic constraints on age and magma genesis of an embryonic oceanic crust: the Chenaillet Ophiolite in the Western Alps. Lithos 160, 283–291.

Lin, J., Purdy, G.M., Schouten, H., Sempéré, J.-C., Zervas, C., 1990. Evidence from gravity data for focused magmatic accretion along the Mid-Atlantic Ridge. Nature 344, 627–632.

Lonsdale, P., 1977. Structural geomorphology of a fast-spreading rise crest: the East Pacific Rise near 3°25'S. Mar. Geophys. Res. 3, 251–293.

Lonsdale, P., 1989. Segmentation of the Pacific-Nazca spreading center, 1°N-20°S. J. Geophys. Res. 94, 12197–12225.

MacDonald, K.C., 1982. Mid-ocean ridges: fine scale tectonic, volcanic and hydrothermal processes within the plate boundary zone. Annu. Rev. Earth Planet Sci. 10 (1), 155–190.

MacDonald, K.C., Fox, P.J., 1988. The axial summit graben and cross-sectional shape of the East Pacific Rise as indicators of axial magma chambers and recent volcanic eruptions. Earth Planet Sci. Lett. 88, 119–131.

Macleod, C.J., Searle, R.C., Murton, B.J., Casey, J.F., Mallows, C., Unsworth, S.C., Achenbach, K.L., Harris, M., 2009. Life cycle of oceanic core complexes. Earth Planet Sci. Lett. 287, 333–344.

Maffione, M., Morris, A., Anderson, M.W., 2013. Recognizing detachment-mode seafloor spreading in the deep geological past. Sci. Rep. 3 https://doi.org/10.1038/srep02336.

Mallows, C, Searle C, R, 2012. A geophysical study of oceanic core complexes and surrounding terrain, Mid-Atlantic Ridge 13°N–14°N. Geochemistry. Geophysics. Geosystems 13 (6). https://doi.org/10.1029/2012GC004075.

Manatschal, G., Sauter, D., Karpoff, A.-M., Masini, E., Mohn, G., Lagabrielle, Y., 2011. The chenaillet ophiolite in the French/Italian Alps: an ancient analogue for an oceanic core complex? Lithos 124 (3–4), 169–184.

Michael, P.J., Langmuir, C.H., Dick, H.J.B., Snow, J.E., Goldstein, S.L., Graham, D.W., Lehnert, G., Kurras, G., Jokat, R., Mühe, R., Edmonds, H.N., 2003. Magmatic and amagmatic seafloor generation at the ultraslow-spreading Gakkel ridge, Arctic Ocean. Nature 423, 956–961.

Miranda, E.A., Dilek, Y., 2010. Oceanic core complex development in modern and ancient oceanic lithosphere: gabbro-localized versus peridotite-localized detachment models. J. Geol. 118 https://doi.org/10.1086/648460.

Nicolas, A., Boudier, F., Ceuleneer, G., 1988. Mantle flow patterns and magma chambers at ocean ridges: evidence from the Oman ophiolite. Mar. Geophys. Res. 9 (4), 293–310.

Nicolas, A., Boudier, F., 1995. Mapping oceanic ridges segments in Oman ophiolite. Journal of Geophysical Research – Solid Earth 100 (B4), 6179–6197.

Ohara, Y., Stern, R.J., Ishii, T., Yurimoto, H., Yamazaki, T., 2002. Peridotite from the Mariana Trough: first look at the mantle beneath an active back-arc basin. Contribution to mineralogy and petrology 143, 1–18.

Passchier, C.W., Trouw, R.A., 2005. Microtectonics. Springer Science & Business Media.

Parnell-Turner, R., Escartín, J., Olive, J.M., Smith, D.K., Petersen, S., 2018. Genesis of corrugated fault surfaces by strain localization recorded at oceanic detachments. Earth Planet Sci. Lett. 498, 116–128.

Perfit, M.R., Fornari, D.J., Smith, M.C., Bender, J.F., Langmuir, C.H., Haymon, R.M., 1994. Small-scale spatial and temporal variations in mid-ocean spatial and temporal variations in mid-ocean ridge crest magmatic processes. Geology 22, 375–379.

Perfit, M.R., Chadwick, W.W., 1998. Magmatism at mid-ocean ridges: constraints from volcanological and geochemical investigations. Faulting and magmatism at Mid-Ocean Ridges – Geophysical Monograph 106, 59–115.

Petit, J.-P., 1987. Criteria for the sense of movement on fault surfaces in brittle rocks. J. Struct. Geol. 9 (5–6), 597–608.

Pitman, W.C., Herron, E.M., Heirtzler, J.R., 1968. Magnetic anomalies in the Pacific and sea floor spreading. J. Geophys. Res. 73 (6), 2069–2085 doi., org/10.1029/JB073i006p02069.

Poliakov, A.N.B., Buck, W.R., 1998. Mechanics of stretching elastic-plastic-viscous layers: applications to slow-spreading mid-ocean ridges. Faulting and Magmatism at Mid-Ocean Ridges Geophysical Monograph 106, 305–324.

Rabinowicz, M., Ceuleneer, G., Nicolas, A., 1987. Melt segregation and flow in mantle diapirs below spreading centers: evidence from the Oman ophiolite. J. Geophys. Res.: Solid Earth 92 (B5), 3475–3486.

Reston, T.J., Ranero, C.R., 2011. The 3-D geometry of detachment faulting at mid-ocean ridges. G-cubed 12 (7), 19p. https://doi.org/10.1029/2011GC003666.

Sauter, D., Cannat, M., Rouméjon, S., Andréani, M., Birot, D., Bronner, A., Brunelli, D., Carlut, J., Delacour, A., Guyader, V., MacLeod, C.J., Manatschal, G., Mendel, V., Ménez, B., Pasini, V., Ruellan, E., Searle, R., 2013. Continuous exhumation of mantle-derived rocks at the Southwest Indian Ridge for 11 million years. Nat. Geosci. 6, 314–320. https://doi.org/10.1038/NGEO1771.

Scheirer, D.S., Macdonald, K.C., 1993. Variation in cross-sectional area of the axial ridge along the East Pacific Ridge: evidence for the magmatic budget of a fast spreading center. J. Geophys. Res. 98, 7871–7885.

Smith, D.K., Cann, J.R., 1999. Constructing the upper crust of the Mid-Atlantic Ridge: a reinterpretation based on the Puna ridge, Kilauea volcano. J. Geophys. Res. 104 (B11), 379. https://doi.org/10.1029/1999JB900177.

Stern, R.J., Bloomer, S.H., Martinez, F., Yamazaki, T., Harrison, T.M., 1996. The composition of back-arc basin lower crust and upper mantle in the Mariana Trough: a first report. Isl. Arc 5 (3), 354–372.

Tucholke, B.E., Lin, J., 1994. A geological model for the structure of ridge segments in slow spreading ocean crust. J. Geophys. Res.: Solid Earth 99 (B6), 11937–11958.

Tucholke, B.E., Lin, J., Kleinrock, M.C., 1998. Megamullions and mullion structures defining oceanic metamorphic core complexes on the Mid-Atlantic Ridge. J. Geophys. Res. 103, 9857–9866.

Tucholke, B.E., Behn, M.D., Buck, W.R., Lin, J., 2008. Role of melt supply in oceanic detachment faulting and formation of megamullions. Geology 36, 455–458, 1030/G24639A.1.

Turcot, E., Macchiavelli, C., Mazzoli, S., Schettino, A., Pierantoni, P.P., 2012. Kinematic evolution of Alpine Corsica in the frame work of Mediterranean mountain belts. Tectonophysics 579, 193–206.

Wallace, R.E., 1951. Geometry of shearing stress and relation to faulting. J. Struct. Geol. 59, 118–130.

Whitehead, J.A., Dick, H.J.B., Schouten, H., 1984. A mechanism for magmatic accretion under spreading center. Nature 312 (8), 146–148.

Whitney L, D, Teyssier, C, Rey, P, Buck R, W, 2013. Continental and oceanic core complexes. GSA Bulletin 125 (3–4), 273–298. https://doi.org/10.1130/B30754.1.